New Journal of Physics

The open access journal at the forefront of physics





PAPER • OPEN ACCESS

Nonadiabatic decay of metastable states on coupled linear potentials

To cite this article: Alisher Duspayev et al 2022 New J. Phys. 24 053043

View the article online for updates and enhancements.

You may also like

- Room-temperature Bloch oscillations and interminiband Zener tunneling in a GaAsbased narrow-minigap superlattice Takeya Unuma, Yuto Itagaki and Soichiro Asakura
- High-field transport in graphene: the impact of Zener tunneling Gaston Kané, Michele Lazzeri and Francesco Mauri
- Landau-Zener tunnelling in 2D periodic structures in the presence of a gauge field: I. Tunnelling rates Andrey R Kolovsky

New Journal of Physics

The open access journal at the forefront of physics



Published in partnership with: Deutsche Physikalische Gesellschaft and the Institute of Physics



OPEN ACCESS

RECEIVED

16 February 2022

REVISED

REVISED 18 April 2022

ACCEPTED FOR PUBLICATION

4 May 2022

PUBLISHED 19 May 2022

Original content from this work may be used under the terms of the Creative Commons Attribution 4.0 licence

Any further distribution of this work must maintain attribution to the author(s) and the title of the work, journal citation and DOI.



PAPER

Nonadiabatic decay of metastable states on coupled linear potentials

Alisher Duspayev^{1,*}, Ansh Shah¹ and Georg Raithel

Department of Physics, University of Michigan, Ann Arbor, MI 48109, United States of America

- * Author to whom any correspondence should be addressed.
- ¹ AD and AS contributed equally to this work.

E-mail: alisherd@umich.edu

Keywords: nonadiabatic decay, quantum dynamics, avoided crossing, Schrodinger equation, Breit-Wigner formula, Landau-Zener tunneling, Fermi's golden rule

Abstract

Avoided crossings of level pairs with opposite slopes can form potential-energy minima for the external degree of freedom of quantum particles, giving rise to metastable states on the avoided crossings (MSACs). Nonadiabatic decay of MSACs is studied by solving the two-component Schrödinger equation in diabatic and adiabatic representations. Non-perturbative lifetime values are found by evaluating wave function flux and scattering phases of time-independent solutions, as well as wave-function decay of time-dependent solutions. The values from these methods generally agree well, validating the utilized approaches. As the adiabaticity parameter, V, of the system is increased by about a factor of ten across the mixed diabatic/adiabatic regime, the MSAC character transitions from marginally to highly stable, with the lifetimes increasing by about ten orders of magnitude. The dependence of MSAC lifetime on the vibrational quantum number, ν , is discussed for several regimes of V. Time-dependent perturbation theory yields lifetimes that deviate by $\lesssim 30\%$ from non-perturbative results, over the range of V and ν studied, while a semi-classical model based on Landau–Zener tunneling is up to a factor of twenty off. The results are relevant to numerous atomic and molecular systems with metastable states on intersecting, coupled potential energy curves.

1. Introduction

Potential wells emerging from two intersecting diabatic potentials with opposite slopes, coupled by an (approximately) constant interaction, are abound in physics and chemistry [1, 2]. Examples include atom traps in optical lattices with Raman couplings [3–6], confinement of Bose–Einstein condensates on radio-frequency-dressed (RF-dressed) magnetic potentials with spin-dependent slopes [7-10], atom trapping in general [11-13], atom interferometry in RF-dressed magnetic guiding potentials [14-17], dressed atom-RF-field states in cavity quantum electrodynamics [18, 19], Rydberg atoms in external fields [20–22], and intersecting potential energy curves (PECs) with radially dependent adiabatic electronic states in Rydberg-Rydberg [23, 24], Rydberg-ground [23, 25] and Rydberg-ion [26-29] molecules. If the slopes of the diabatic potentials have opposite signs, the upper adiabatic potential surface exhibits a potential well. The classical motion in such adiabatic-potential wells is a bound, periodic oscillation about the avoided crossing. The semi-classical Landau-Zener (LZ) tunneling equation [30, 31] has sometimes been applied to estimate the nonadiabatic decay rates of analogous quantum states in adiabatic-potential wells. The LZ estimates are exponentially dependent on several parameters, including a fixed, classical mass-point velocity that must be estimated based on the vibrational quantum motion. LZ estimates of nonadiabatic decay rates of quantum states with low vibrational quantum numbers can differ significantly from their true quantum-mechanical values [13, 29].

In this paper, we present a non-perturbative quantum-mechanical analysis of nonadiabatic decay of low-lying metastable states at avoided crossings (MSACs). Similar descriptions have previously been

A Duspayev et al

employed to model wave-packet dynamics on intersections [13, 32] and in Rydberg-ground molecules [33, 34]. Here, we concentrate on the nonadiabatic lifetimes of quasi-stationary MSACs, which are important in the aforementioned applications. After explaining our model and the utilized techniques in section 2, in section 3 we obtain solutions of the time-dependent Schrödinger equation (TDSE) and time-independent Schrödinger equations (TIDSEs) in both diabatic and adiabatic representations. We extract nonadiabatic MSAC lifetimes from six non-perturbative methods, and compare and interpret the results. The analysis is performed for a range of coupling strengths between the diabatic potentials, for MSACs with vibrational quantum numbers ranging up to about 15. In section 4, we compare the non-perturbative MSAC lifetime results with estimates based on time-dependent perturbation theory, and with semi-classical estimates based on the LZ formula. The paper is concluded in section 5.

2. Methods

2.1. System under study

In the system of interest, the physical Hamiltonian in the diabatic representation,

$$\hat{H}_p = -\frac{\hbar^2}{2M} \begin{pmatrix} \frac{\mathrm{d}^2}{\mathrm{d}x_p^2} & 0\\ 0 & \frac{\mathrm{d}^2}{\mathrm{d}x_p^2} \end{pmatrix} + \begin{pmatrix} -\frac{\alpha_p}{2}x_p & V_p\\ V_p & \frac{\alpha_p}{2}x_p \end{pmatrix},\tag{1}$$

acts on a two-component wave function $(\psi_1(x), \psi_2(x))$ with a position-independent, internal state space denoted as $\{|1\rangle, |2\rangle\}$, in that order. The constants α_p and V_p are chosen positive and real. The effective particle mass is denoted M, and the external degree of freedom has a spatial coordinate x_p . The diabatic energies of the internal states $\{|1\rangle, |2\rangle\}$ as a function of x_p are $V_1 = -\alpha_p x_p/2$ and $V_2 = \alpha_p x_p/2$, respectively, with differential slope α_p , and the constant coupling between these states is V_p .

For convenient description of different physical systems, we use the following units for length, energy, time and frequency,

Length:
$$l_0 = \sqrt[3]{\frac{\hbar^2}{M\alpha_p}}$$

Energy: $w_0 = \frac{\hbar^2}{Ml_0^2}$
Time: $t_0 = \frac{\hbar}{w_0}$
Frequency: $f_0 = \frac{w_0}{\hbar}$ (2)

Expressing length and energy in these units, the Hamiltonian in equation (1) transforms into the scaled Hamiltonian in diabatic representation,

$$\hat{H}_{D} = -\frac{1}{2} \begin{pmatrix} \frac{d^{2}}{dx^{2}} & 0\\ 0 & \frac{d^{2}}{dx^{2}} \end{pmatrix} + \begin{pmatrix} -\frac{1}{2}x & V\\ V & \frac{1}{2}x \end{pmatrix}, \tag{3}$$

with scaled position $x = x_p/l_0$ and scaled coupling strength

$$V = \frac{V_p}{w_0}. (4)$$

The characteristic half width of the crossing region in scaled units (s.u.) is $x_w = 2V$; in physical length units it is $x_{wp} = Vl_0 = 2V_p/\alpha_p$. The scaled coupling V serves as an adiabaticity parameter: the larger V, the more adiabatic a system will behave, and the less affected the MSACs will be by nonadiabatic decay. In the following, we will use the s.u. defined in equation (2).

The x-dependent adiabatic-state basis $\{|u\rangle, |d\rangle\}$ for the internal degree of freedom, and the adiabatic potentials V_u and V_d , are defined by $\hat{H}_D|u\rangle = V_u(x)|u\rangle$ and $\hat{H}_D|d\rangle = V_d(x)|d\rangle$, with u and d standing for 'up' and 'down' in energy, V_u positive, and $V_d = -V_u$. With the notation $|u\rangle(x) = \sum_{i=1,2} \chi_{u,i}(x)|i\rangle$ and

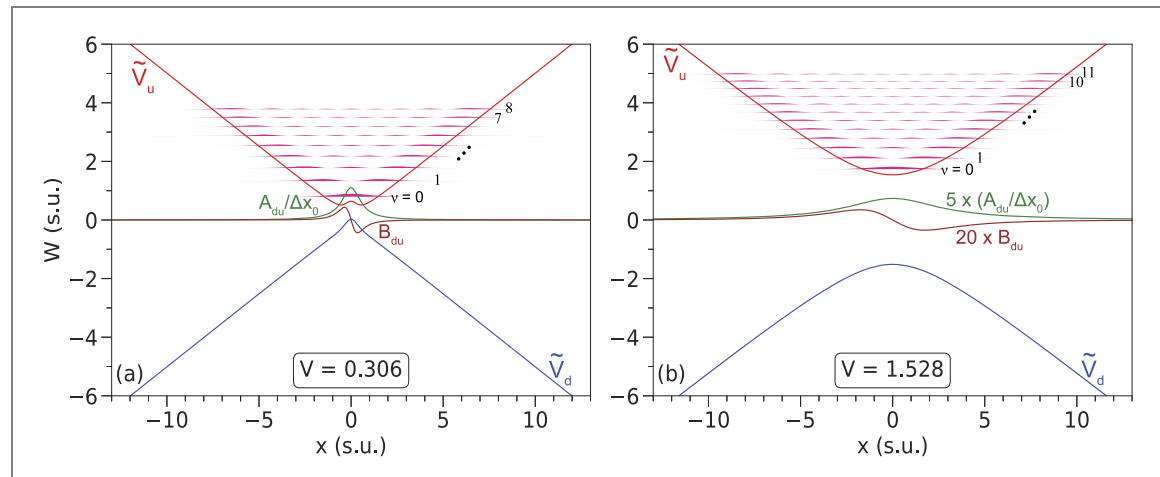


Figure 1. PECs and nonadiabatic couplings in the Hamiltonian in equation (6) for the cases V=0.306 (a) and V=1.528 (b). In order to show the first-order coupling, A_{du} , on a physically relevant energy scale, we plot A_{du} divided by the position uncertainty of the ground state in harmonic approximation, $\Delta x_0 = V^{1/4}$. Note the scaling factors for the nonadiabatic couplings in (b). The wave-function densities of the lowest 9 (a) and 12 (b) MSACs are also shown. The baselines of the individual wave function plots correspond with the respective resonance energies, W_{ν} , on the vertical axis.

 $|d\rangle(x) = \sum_{i=1,2} \chi_{d,i}(x)|i\rangle$, the first- and second-order nonadiabatic couplings are

$$A_{\alpha,\beta}(x) = -\sum_{i=1,2} \chi_{\alpha,i}^*(x) \frac{\mathrm{d}}{\mathrm{d}x} \chi_{\beta,i}(x)$$

$$B_{\alpha,\beta}(x) = -\frac{1}{2} \sum_{i=1,2} \chi_{\alpha,i}^*(x) \frac{\mathrm{d}^2}{\mathrm{d}x^2} \chi_{\beta,i}(x). \tag{5}$$

There, the index i denotes diabatic and the Greek letters denote adiabatic basis states. The $\chi_{\alpha,i}$ can be chosen real. The 2×2 matrix $A_{\alpha,\beta}$ then is anti-symmetric at any value of x, with α and β being u or d. The diagonal elements of $B_{\alpha,\beta}(x)$ are compounded with the adiabatic potentials to yield the PECs $\tilde{V}_{\alpha}(x) = V_{\alpha}(x) + B_{\alpha,\alpha}(x)$, with $\alpha = u$ or d. The adiabatic Hamiltonian, which is a special case of the Born–Huang representation [35, 36] for the case studied in our paper, then writes

$$\hat{H}_{A} = -\frac{1}{2} \begin{pmatrix} \frac{d^{2}}{dx^{2}} & 0\\ 0 & \frac{d^{2}}{dx^{2}} \end{pmatrix} + \begin{pmatrix} \tilde{V}_{u}(x) & 0\\ 0 & \tilde{V}_{d}(x) \end{pmatrix} + \begin{pmatrix} 0 & B_{ud}(x) + A_{ud}(x) \frac{d}{dx}\\ B_{du}(x) - A_{ud}(x) \frac{d}{dx} & 0 \end{pmatrix}. \quad (6)$$

This Hamiltonian acts on the adiabatic wave functions, $(\psi_u(x), \psi_d(x))$. As visualized in figure 1, the nonadiabatic *A*- and *B*- couplings vanish for $x \gg V$, with *V* from equations (3) and (4).

2.2. Time-independent solutions

2.2.1. Diabatic representation

A straightforward method to arrive at a non-perturbative solution is to solve the TIDSE for the Hamiltonian from equation (3). Here, we are interested in the energy range W > V, where MSAC resonances exist. The MSAC resonance energies and corresponding two-component wave functions are obtained numerically. As a spatial integration method, we have chosen a 4th order Runge–Kutta method, which allows for first-derivative terms (needed in the adiabatic representation discussed in section 2.2.2). In the following, relevant details are explained.

It is well-known from textbooks that for a spin-less particle on a linear potential the wave-function solutions are given by Airy functions (see, e.g. [37]). In the case of two coupled linear potentials, as in equation (3), the matching of the boundary conditions in the classically forbidden regions turns out to be numerically delicate due to the coupling V between the classically-allowed, Airy-function-like solutions to the co-located classically forbidden ones. In the asymptotic regions, the allowed solutions are, locally, approximately given by $a(x)\cos(kx+\phi)$, with a slowly-varying local amplitude a(x), wave number $k(x)=\sqrt{2(|x|/2+W)}$, the quantum state's scaled energy W, and a phase ϕ . For large |x|, the classically-forbidden solutions are then approximately given by $-\frac{a(x)V}{|x|/2+W}\cos(kx+\phi)$. The amplitudes of the forbidden solutions drop off quite slowly in |x|, because V is fixed and never 'turns off'. In the numerical implementation, this exacerbates the tendency of the classically-forbidden solutions to

exponentially diverge at large |x|. The issue is addressed by choosing sufficiently small values for the spatial step size, Δx , and for the slope iteration parameter, s, explained in the next paragraph. The issue is less pronounced in the adiabatic approach, because the nonadiabatic A- and B-couplings both do 'turn off' at large |x| (see section 2.2.2).

The energy spectrum of the Hamiltonian in equation (3) is continuous and ranges from $-\infty$ to ∞ . The numerical treatment is simplified by the symmetry of the real-valued solutions. For each energy W there exists an even and an odd solution. Even solutions, which are associated with even-parity MSACs, are of the form $\psi_1(x) = 1 - sx$ and $\psi_2(x) = 1 + sx$ for $|x| \to 0$, with a slope parameter s. The odd solutions are of the form $\psi_1(x) = 1 + sx$ and $\psi_2(x) = -1 + sx$ for $|x| \to 0$. Further, for any s it is $\psi_2(-x) = \psi_1(s)$ for the even and $\psi_2(-x) = -\psi_1(s)$ for the odd solutions. For any energy s, this leaves only one parameter—the slope s—to be iterated. In both even and odd cases, the slope parameter s is iterated to minimize the classically forbidden wave-function components at the spatial-range limit, $|s| = s_{max}$. We vary s_{max} depending on s0 and s1 and s2 as to allow for maximum outward propagation before the wave functions diverge due to numerical inaccuracies. For each energy s3, this procedure yields exactly one even and one odd physical solution.

2.2.2. Adiabatic representation

The TIDSE in the adiabatic picture has the Hamiltonian from equation (6). The even adiabatic solutions are of the form $\psi_u(x) = 1$ and $\psi_d(x) = sx$ for $|x| \to 0$, and the odd ones are of the form $\psi_u(x) = sx$ and $\psi_d(x) = 1$ for $|x| \to 0$. As in section 2.2.1, the slope parameter s is iterated to minimize the classically forbidden wave-function components $\psi_u(x)$ at the spatial-range limits, $|x| = x_{\text{max}}$. For each energy value W, there exist exactly one even and one odd solution. In the numerical treatment, the tendency of the classically forbidden solutions on the respective PECs to exponentially diverge at large |x| is less pronounced in the adiabatic representation than it is in the diabatic representation (section 2.2.1), because the nonadiabatic A- and B-couplings 'turn off' at large |x|, whereas in the diabatic representation the constant coupling V does not 'turn off' at large |x|.

2.2.3. MSAC resonances

The energies W_{ν} of the MSAC resonances, labeled by an integer vibrational quantum number ν , can be determined iteratively by locating the energy values at which the amplitudes of the sinusoidal wave-function tails in the respective classically-forbidden regions become minimal near the edges of the spatial integration range, $|x|=x_{\rm max}$. We label the resonances starting with $\nu=0$ for the MSAC ground state. The coupling parameter V is varied between 0.3 (least adiabatic) and 2.8 (most adiabatic), in s.u. as defined in equations (2) and (4). We find all MSAC resonances within an energy range of about $V < W \lesssim V + 3.8$. For V ranging between 0.3 and 2.8, the number of MSACs with $V < W_{\nu} \lesssim V + 3.8$ ranges from 9 to 15, respectively. The integration limit, $x_{\rm max}$, is shifted outward with increasing V and ν in order to locate the MSAC energies as accurately as possible over the entire V- and ν -range studied. Here, $x_{\rm max}$ is varied between $x_{\rm max}=13$ at the lowest V and ν , and $x_{\rm max}=19$ at the largest V and ν .

For illustration, in figure 1 we show plots of the adiabatic potentials \tilde{V}_d and \tilde{V}_u and the A- and B-potentials for V=0.306 and V=1.5275, as well as the obtained lowest MSACs. In addition to $A_{ud}(x)=-A_{du}(x)$, in the present problem it is also $B_{ud}(x)=-B_{du}(x)$. Figure 1 illustrates the rapid drop in amplitude of both the A- and B-potentials with increasing V. The diagonal B-potentials, $B_{dd}(x)$ and $B_{uu}(x)$, become apparent in the V=0.306-case in the form of small humps on the $\tilde{V}(x)$ in the range $|x|\lesssim 1$. The A-couplings generally appear to be more important than the B-couplings, as confirmed directly in section 4.1 and as commonly accepted in molecular physics. A feature that becomes important in the interpretation of the ν -dependence of the MSAC lifetimes in section 3.2 is that at low V the approximate reach of the A- and B-potentials, given by the crossing half width, $x_w=2V$, is smaller than the typical wave function extents, whereas at large V the A- and B-potentials are spread out over the entire typical wave-function extent.

2.2.4. MSAC lifetimes from flux calculation

The main interest in the present work is in the nonadiabatic lifetime of the lowest MSAC resonances. To that end, we compute even and odd solutions on a dense grid of the continuous energy W, and determine the resonance centers, W_{ν} , as described in section 2.2.3. In either representation, the MSAC resonance centers W_{ν} are found by minimizing the amplitudes of the sinusoidal wave-function tails in the peripheral regions, $|x| \sim x_{\text{max}}$, relative to the wave-function amplitudes in the MSAC trapping region near x=0. As seen in figure 2, in the asymptotic regions both classically allowed and forbidden wave-function tails are locally of the form $\psi(x) = a(x)\cos[k(x)x + \phi(W)]$, with a slowly-varying amplitude a, an energy-dependent phase ϕ , and a slowly-varying wave number k. In the diabatic representation, the oscillatory behavior of the classically-forbidden tails results from the fixed coupling V, which induces π -out-of-phase

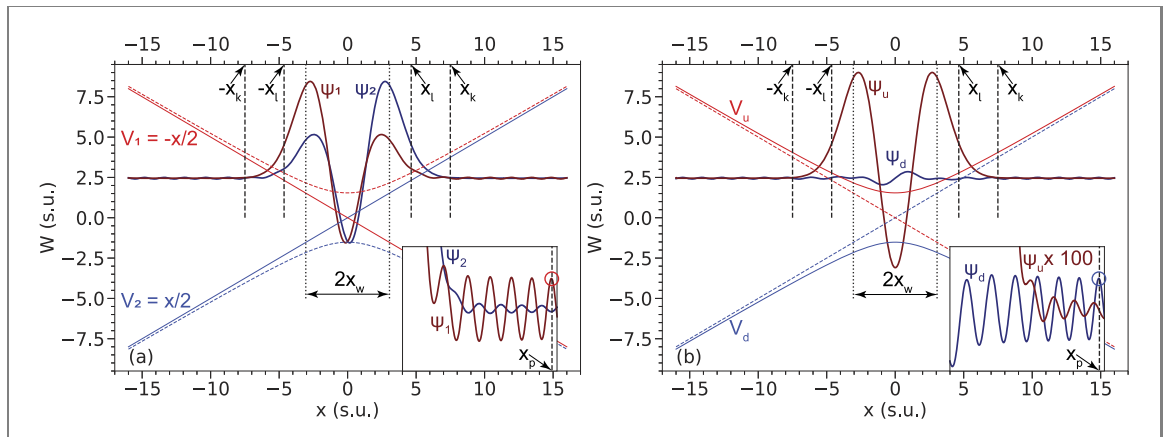


Figure 2. Details for the lifetime calculations in diabatic (a) and adiabatic (b) representations, with diabatic potentials $V_{1/2} = \mp x/2$ and adiabatic potentials V_u and V_d (all quantities in s.u.). The displayed case is for a coupling strength of V=1.5275 s.u.. The wave functions ψ_1 and ψ_2 in (a), and ψ_u and ψ_d in (b), show the vibrational MSAC $\nu=2$. The insets in (a) and (b) show magnified views of the wave-function tails in the classically forbidden regions of the respective higher-energy potentials. Note that ψ_u in the inset in (b) is multiplied by a factor of 100. The markers x_l , x_k and x_w in the main plots as well as x_p and the open circles in the insets are to illustrate details of the flux calculations explained in the text.

classically-forbidden tails. Denoting the amplitude of the classically allowed tail a_a , and that of the co-located classically forbidden tail a_f , at the spatial integration boundary x_{max} the amplitude $a_f \sim \frac{a_a V}{x_{\text{max}}/2+W}$ can be on the order of 10% of a_a (see, for instance, the inset of figure 2(a)). In the adiabatic representation, the oscillatory behavior of the classically-forbidden tails primarily results from the diminishing nonadiabatic A-coupling, which induces $\pi/2$ -out-of-phase forbidden tails with much smaller amplitudes than in the diabatic representation (note that in the inset in figure 2(b) the classically forbidden tail of ψ_u is magnified by a factor of 100).

To explain the flux method, we first consider a scalar problem, in which there is only one internal state. In that case, the steady-state wave-functions in the peripheral regions are superpositions of scalar in-going, reflected and transmitted waves $\propto \exp(\pm ikx)$. At the exact resonance centers, the amplitudes of the peripheral waves are minimal relative to the resonance amplitudes near x = 0, the transmission is unity, and the reflectivity is zero (as is the case, for instance, in quantum double-barrier problems and optical loss-free Fabry-Perot interferometers). A plane transmitted wave of the form $A \exp(ikx)$ at positive x, therefore, corresponds with an incident wave $A_1 \exp(ikx)$ at negative x, with the same magnitude, $|A_1| = |A|$. The resonantly enhanced wave-function near x = 0 symmetrically emits the transmitted wave, $A \exp(ikx)$ for x > 0, as well as a delayed reflected wave $A_{R,Del} \exp(-ikx)$ that perfectly destructively interferes with the direct reflected wave, $A_{R,Dir} \exp(-ikx)$, where $|A| = |A_{R,Del}| = |A_{R,Dir}|$ and $A_{R,Del} = -A_{R,Dir}$. If one were to switch off the incident wave, $A_{\rm I} \exp(ikx)$, the direct reflected wave, $A_{\rm R,Dir} \exp(-ikx)$, would also cease, leaving the delayed reflected and the transmitted waves, which have amplitudes with equal magnitudes |A|. The outgoing flux, $j = \frac{1}{2i}(\psi^* \frac{d}{dx}\psi - \psi \frac{d}{dx}\psi^*)$, summed over the positive- and negative-x domains and after terminating the incident wave, is $2k|A|^2$. Denoting the norm of the resonantly enhanced, trapped wave-function as P_0 , an exponential decay of the resonance norm at a decay rate of $\Gamma = 2k|A|^2/P_0$ occurs. Since P_0 itself is proportional to $|A|^2$, the factor $|A|^2$ drops out at the end of the calculation of Γ .

The analysis presented in the previous paragraph extends to real-valued solutions with peripheral wave-functions of the form $a\cos(\pm kx + \phi)$, obtained in our work, as those can be written as superpositions of complex plane-wave solutions. Therefore, $\Gamma = 2k|a|^2/P_0$. Further, if there are two internal states, as is the case in the present paper, both P_0 and the flux are summed over these states. For the result to be accurate, it is important to first find the resonance center energy, W_{ν} , at which the wave-function tails have minimal amplitudes relative to the trapped wave-function near x=0.

We first discuss the implementation in diabatic representation, in which the norm P_0 of the MSAC wave functions $P_0 = \int_{-x_k}^{x_k} [|\psi_1(x)|^2 + |\psi_2(x)|^2] dx$. We define the integration boundary x_k via $\int_{x_l}^{x_k} k(x) dx = r_k$, where x_l is the positive classical turning point of the state of interest on $V_u(x)$, $x_k > x_l$, and $k(x) = \sqrt{2(V_u(x) - W)}$. In this way, the limit x_k is set such that P_0 captures the decaying tails of the MSAC resonances in the classically-forbidden regions to within r_k semi-classical 1/e decay lengths outside the classical turning points. Here we use $r_k = 3$, which is large enough for P_0 to capture the entire resonance norm, and small enough to not include substantial probability from the oscillatory wave-function tails. The exact value of r_k is not important. Note that we define the boundaries via the upper adiabatic potential, $V_u(x)$, in both the diabatic and adiabatic representations. The limits x_l and x_k are visualized in figure 2.

The amplitudes a_1 and a_2 of the oscillatory wave-function tails are found by first locating a position x_p where the (classically allowed) tail of $\psi_1(x)$ takes an extremal value close to the positive limit of the spatial integration range, x_{max} (see circle in the inset of figure 2(a)). Near x_p , both wave functions $\psi_i(x)$ then are of the form $\psi_i(x) = a_i \cos[k_i(x_p)x + \phi_i]$, with i = 1, 2. Using three adjacent carrier points of each $\psi_i(x)$ with x_p

at the center, we compute the wave numbers $k_i(x_p) = \sqrt{|\frac{\mathrm{d}^2}{\mathrm{d}x^2}\psi_i(x_p)| \over \psi_i(x_p)}|}$ and the amplitudes

 $a_i(x_p) = \sqrt{\psi_i(x_p)^2 + (\frac{\mathrm{d}}{\mathrm{d}x}\psi_i(x_p)/k_i(x_p))^2}$. Due to the position-independence of the diabatic internal states, $\{|1\rangle, |2\rangle\}$, the fluxes in the two wave-function components just add up. The 1/e lifetime $\tau_{\mathrm{nad,FC}} = 1/\Gamma_{\mathrm{nad,FC}}$, obtained from the time-independent MSAC wave function in the diabatic picture, then is given by

$$\tau_{\text{nad,FC}} = \frac{1}{\Gamma_{\text{nad,FC}}} = \frac{P_0}{2(k_1 a_1^2 + k_2 a_2^2)}.$$
 (7)

It is noted that $k_1 \approx k_2$ in all cases, whereas the ratio a_2/a_1 increases with V.

We also obtain the lifetimes in the adiabatic representation, in which the wave-function computation is numerically more stable. The norm integral P_0 is computed with the same boundary x_k as in the diabatic representation, $P_0 = \int_{-x_k}^{x_k} [|\psi_u(x)|^2 + |\psi_d(x)|^2] dx$. We then find a peak location x_p of the (classically-allowed) tail of $\psi_d(x)$ near the integration limit, x_{max} (see circle in the inset of figure 2(b)). In the flux calculation in the adiabatic representation, the x-dependence of the adiabatic internal-state basis $\{|u\rangle(x), |d\rangle(x)\}$ must be considered. This is accomplished by transforming the adiabatic two-component wave function, $(\psi_d(x), \psi_u(x))$, into diabatic representation, $(\psi_1(x), \psi_2(x))$, at three adjacent x-values centered at x_p . The decay rate $\Gamma_{\text{ad,FC}}$ and the 1/e lifetime $\tau_{\text{ad,FC}}$ of the time-independent MSAC wave function in the adiabatic picture are then computed from $(\psi_1(x), \psi_2(x))$ at x_p , using equations from the previous paragraph.

2.2.5. MSAC lifetimes from the Breit-Wigner formula

In an alternative, quite different method, we also obtain the MSAC lifetimes from the Breit–Wigner formula (BW) [38]. In the asymptotic regions, time-independent real-valued solutions on the classically allowed potentials are locally of the form $\psi(x) = a\cos(k(x)x + \phi(W))$, with an energy-dependent phase ϕ . The asymptotic solution is a superposition of incident and back-scattered waves of respective forms $\exp(-ikx)$ and $\exp(i(kx+2\delta))$, with the usual scattering phase shift δ [38]. It is thus seen that the phase ϕ in the time-independent solution equals the scattering phase, $\delta = \phi$. According to the BW formula, the decay rate of a MSAC, at the center of the scattering resonance, is given by $\Gamma_{\rm BW} = 2({\rm d}W/{\rm d}\phi)$, where the derivative is taken at a fixed location $x_{\rm B}$ well outside the classically allowed range of the bound component of the MSAC wave function. Here we pick a location close to $x_{\rm max}$; the exact value of $x_{\rm B}$ is not important. The phase is then obtained from the classically-allowed tails of the wave functions $\psi_1(x)$ or $\psi_d(x)$ at $x_{\rm B}$, in the diabatic and adiabatic representations, respectively, using

$$\phi(W) = \tan^{-1} \left(-\frac{1}{\psi(x_{\rm B})} \frac{\mathrm{d}\psi(x)}{\mathrm{d}x} \Big|_{x=x_{\rm R}} \right) + m\pi, \tag{8}$$

where the integer m is continually adjusted as a function of W for continuity of $\phi(W)$. We subtract a background phase $\phi_0(W)$ that arises from the phase shift of the non-resonant solutions away from the MSACs and that is computed from

$$\phi_0(W) = \int_0^{x_{\rm B}} \sqrt{2(W - V_*(x))} \mathrm{d}x,\tag{9}$$

where the potential $V_*(x) = -x/2$ in the diabatic and $V_*(x) = V_d(x)$ in the adiabatic representation. Note that for vanishing coupling, V = 0, the phase would be that of an Airy-function solution [37]). The BW decay rates and lifetimes then become

$$\tau_{*,BW} = \frac{1}{\Gamma_{*,BW}} = 2\frac{d(\phi_* - \phi_{*,0})}{dW},$$
(10)

where * = nad and * = ad for the diabatic and adiabatic representation, respectively.

In summary of this subsection, we obtain four values for the nonadiabatic decay times of MSACs from solutions of time-independent two-component Schrödinger equations in diabatic and adiabatic representation, namely $\tau_{\text{nad},\text{FC}}$, $\tau_{\text{nad},\text{BW}}$, $\tau_{\text{ad},\text{FC}}$, and $\tau_{\text{ad},\text{BW}}$. As expected and shown below, these generally agree very well with each other, with the values from the adiabatic picture being more accurate due to the vanishing of the A- and B-coupling terms at large |x|.

2.3. Time-dependent methods

In our time-dependent computations, we utilize the scaled Hamiltonians in equations (3) and (6) from section 2.2 to find the MSAC lifetimes by propagating MSAC wave functions. For instance, in the adiabatic representation the TDSE reads

$$i\frac{\partial\psi_{d}(x,t)}{\partial t} = -\frac{1}{2}\frac{\partial^{2}\psi_{d}(x,t)}{\partial x^{2}} + \tilde{V}_{d}(x)\psi_{d}(x,t) + \left[B_{du}(x) + A_{du}(x)\frac{\partial}{\partial x}\right]\psi_{u}(x,t)$$

$$i\frac{\partial\psi_{u}(x,t)}{\partial t} = -\frac{1}{2}\frac{\partial^{2}\psi_{u}(x,t)}{\partial x^{2}} + \tilde{V}_{u}(x)\psi_{u}(x,t) + \left[B_{ud}(x) - A_{du}(x)\frac{\partial}{\partial x}\right]\psi_{d}(x,t). \tag{11}$$

In addition to $A_{ud}(x) = -A_{du}(x)$, in the present problem we also have $B_{ud}(x) = -B_{du}(x)$ for all x. The TDSE in diabatic representation follows from equation (3).

As initial conditions for the MSAC wave functions at time t=0 in the diabatic and the adiabatic representations, we use the respective time-independent solutions obtained in section 2.2.3. The MSAC wave functions from section 2.2.3 exhibit oscillatory tails near the boundaries of the integration grid, as seen in figure 2. To avoid numerical instability, the MSAC wave functions entered as initial states are set to zero between their outermost nodes and the respective spatial integration boundaries, $\pm x_{max}$.

At the core of the TDSE method is to absorb the outgoing flux and to eliminate reflections from the boundaries [39]. The wave-function norms then drop exponentially, thereby revealing the decay time of the MSAC entered as initial state. The absorption is implemented by padding all diagonal potentials with imaginary absorbing layers near the spatial integration boundaries at $\pm x_{\text{max}}$. The absorbing layers rise smoothly from zero at locations well-outside the classical turning points, $\pm x_l$, to a maximal value at $\pm x_{\text{max}}$. The utilized time-propagation method is a Crank–Nicolson scheme [40] that is similar to schemes used in our recent work on tractor atom interferometry [41] and Rydberg-ion molecules [29], where nonadiabatic transitions were quantitatively described. More details on the method can be found there. In the present work, the time-dependent computations are performed with a spatial-grid step size of $\Delta x = 10^{-3}$, the same as in the time-independent methods described in section 2.2, and a time-step size of $\Delta t = 10^{-3}$ (all in s.u.). We have checked that a reduction of Δt does not significantly affect the lifetimes found for the MSAC wave functions. The TDSE computations in the diabatic and adiabatic representations yield MSAC lifetimes denoted $\tau_{\text{nad,TDSE}}$ and $\tau_{\text{ad,TDSE}}$, respectively.

3. Results

3.1. Comparison of methods

In figure 3(a), we first present a comparison of results for a moderately adiabatic case, V=1.528, for $\nu=0$ to 11. The log-scale plot shows excellent agreement of lifetime data from all six methods over the entire range of ν , over which the lifetime drops by about a factor of 30. Among the methods, we consider the adiabatic wave-function flux results, $\tau_{\rm ad,FC}$, to be the most accurate and precise for the following reasons. The adiabatic analysis is less prone to numerical inaccuracy in the classically-forbidden tails of the wave functions, because the adiabatic couplings A and B drop off rapidly with increasing |x| (see figures 1 and 2, and arguments presented in section 2.2). This reduces the amplitude of the classically-forbidden tails, thereby alleviating their tendency towards exponential divergence. Further, the flux method is insensitive to background-phase effects, which affects the BW method at low V (see section 3.2).

To exhibit small deviations of the results of the other five methods from $\tau_{\rm ad,FC}$, in figure 3(b) we show the ratios $\tau_*/\tau_{\rm ad,FC}$, with * denoting the other methods. Importantly, the values for τ deviate by no more than 11% from $\tau_{\rm ad,FC}$. The four results from the TIDSE agree to within 2% from each other, for V=1.528, with small deviations attributed to numerical inaccuracy and to the systematic inaccuracy of the BW method at low V (see section 3.2). The computations based on the TDSE deviate by up to 11% from $\tau_{\rm ad,FC}$. This may be due to the susceptibility of the time-dependent computations to imperfections of the absorbing-wall implementation, such as less-than-perfect absorption of the outgoing flux and spurious reflections. Indeed, for $\nu \leqslant 4$, where the absorbing walls are the farthest away from the high-amplitude regions of the MSAC wave functions, the TDSE lifetime results deviate by less than about 5% from the TIDSE results. It is also noted that the diabatic and adiabatic TDSE calculations differ by less than about 1% from each other for all ν -values. This indicates that numerical issues, such as spatial-step or time-step sizes, introduce about the same, %-level of uncertainty in the TDSE and the TIDSE calculations.

Overall, the close agreement across the six methods in figure 3 proves the fundamental validity of all methods used. The quite good agreement between the TDSE and TIDSE calculations provides a particularly high level of validation, as the methods of how to extract the lifetimes from the TDISE and TDSE computations are quite different, yet both approaches yield very similar results.

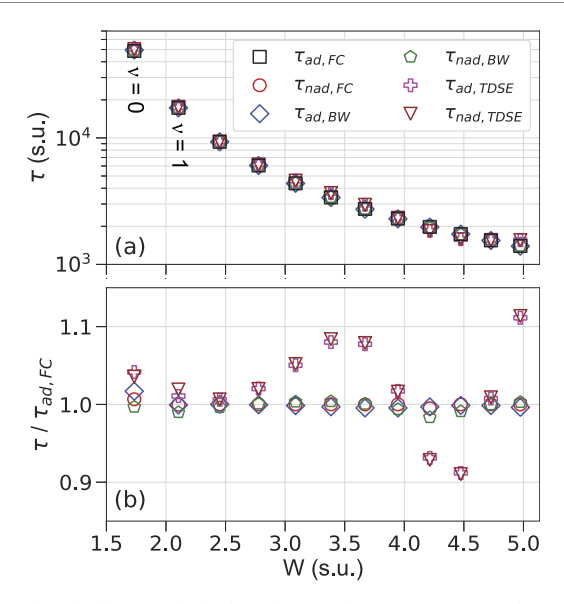


Figure 3. MSAC lifetimes obtained with all six methods, for vibrational states $\nu=0$ to 11, for an intermediate case of the coupling strength (V=1.5275 s.u.), plotted vs MSAC level energy W. The top panel demonstrates the overall agreement between all data and the drop-off of the lifetimes as a function of ν . For improved visualization of small deviations, in the lower panel we show the ratios between the lifetimes from five methods relative to $\tau_{\rm ad,FC}$.

3.2. Lifetimes vs adiabaticity

A main outcome of the work are the MSAC lifetimes over a wide range of the adiabaticity V and the vibrational quantum number ν . We have performed computations for a set of V-values ranging from V=0.306 (least adiabatic) to V=2.75 (most adiabatic). To assist with the interpretation of various regimes, we define the quality factor, Q, of the resonances as the angular frequency in harmonic approximation times the state's norm divided by the time derivative of the norm, or $Q=\tau\omega=\tau/(2\sqrt{V})$. There, ω is evaluated from the adiabatic potential $V_u(x)$ near x=0. Note Q is unit-less and the same in scaled and physical units.

In figure 4(a) we show the Q-values for the MSAC vibrational ground state, $\nu=0$, versus V. Noting that the number of oscillations after which the survival probability drops below 50% is approximately Q/9, it is seen that the ground-state MSACs may be considered only barely oscillatory for $0.3 < V \lesssim 0.6$, as in these cases it only takes a few oscillation periods or less for half of the ground-state MSAC population to decay. For $V \approx 1$ it already takes a few tens of oscillation periods before the ground-state MSACs are half decayed. However, as V rises above about a value of 2, the ground-state MSACs quickly become highly stable against nonadiabatic decay. At the largest V-value tested, V=2.75, it takes V=0.90 oscillation periods for half of the ground-state MSAC population to nonadiabatically decay (see figure 4(a)). The rapid stabilization of MSACs as a function of V1 is related to the factor of V2 in the exponential expression for the LZ tunneling probability (see section 4.2).

The wide range of MSAC level damping is further visualized in figure 4(b), where we show four examples of the wave-function scattering phases, $\phi(W) - \phi_0(W)$, that are used for the calculation of BW lifetimes according to section 2.2.5. At the MSAC energies, W_{ν} , the phases exhibit rises in steps of π . The energy widths of the rises drop from a large fraction of the level spacing at V=0.306 to too narrow to be visible at V=2.444. Figure 4(b) reiterates the vast range of nonadiabatic damping behavior that is seen over the range 0.3 < V < 2.444, a range over which V varies by about one and Q by about ten orders of magnitude.

Figure 4(b) also shows that at the lowest V-values the resonances are wide enough and the slopes at the resonances, $d(\phi - \phi_0)/dW$, are small enough that background trends and cross talk between neighboring MSACs will affect the $d(\phi - \phi_0)/dW$ -readings at the resonance centers, W_{ν} . This makes lifetimes from the BW formula inaccurate at low V, as seen below. Lifetimes from flux calculations are not susceptible to this type of inaccuracy.

In figure 5 we show lifetime results from TIDSE computations for ten values of V for MSACs within an energy range of about 3.8 s.u. from the potential minima of V_u . (The computationally more intensive TDSE computations were performed only for the intermediate case of V=1.528.) Figure 5(a) demonstrates good agreement between the TIDSE methods over a wide range of conditions. For all ν -values studied, the MSAC lifetimes increase by six to ten orders of magnitude, as V is increased from 0.306 to 2.75. In the following, we discuss the dependence of the lifetimes on ν in several regimes of V.

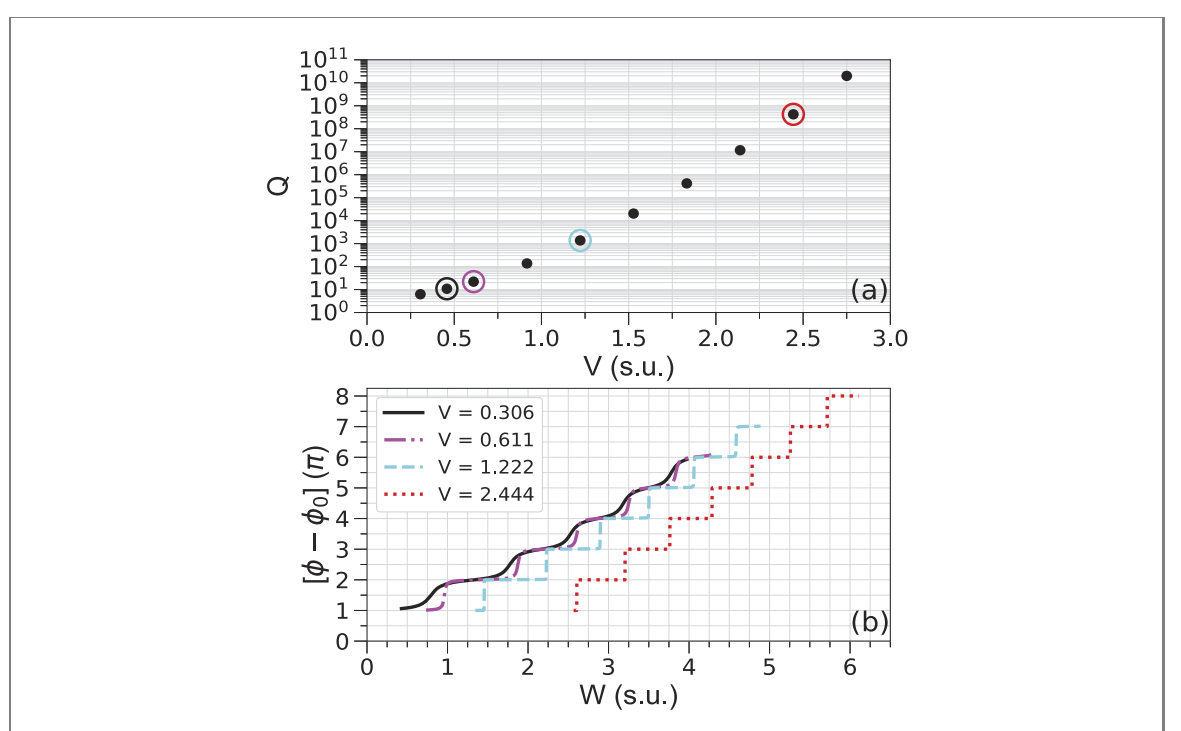


Figure 4. (a) Quality factors, Q, as defined in the text, for the MSAC ground states, $\nu=0$, vs coupling strength V. Circles around data points indicate the cases selected for panel (b). (b) Wave-function phases, $\phi(W)-\phi_0(W)$, vs energy for four values of V selected in panel (a).

In the nonadiabatic regime, $V \lesssim 0.6$, the lifetime barely depends on the vibrational quantum number, ν , and for the least-adiabatic case, V=0.306, the lifetime actually increases with ν . This behavior, which may seem counter-intuitive at first, reflects the fact that for $V \ll 1$ the anti-crossing half width, $x_w=2V$, which is an estimate for the reach of the A- and B-couplings, only is a fraction of the spatial extent of the MSAC wave function on \tilde{V}_u , as seen above in figure 1(a). As a result, for $V \ll 1$ the spatial extent of the interaction range that causes the nonadiabatic decay, measured relative to the wave-function extent, decreases with increasing ν , leading to an increase in lifetime with increasing ν . This mechanism becomes more transparent in an analysis based on Fermi's golden rule (FGR) (see section 4.1). Arguing semi-classically, one may say that at the lowest V-values studied the lifetime increases with ν because with increasing ν the MSAC particle spends less of its time in the anti-crossing region. It is noted that increasing ν for the purpose of increasing the MSAC lifetime is not a useful concept to generate long-lived MSACs (for atom trapping, for instance), because of the generally very low Q-values at $V \lesssim 0.6$ (see figure 4(a)).

For $V \gtrsim 1.2$, the MSAC resonances become increasingly adiabatic, with Q-values beginning to range above 100. In the adiabatic regime, the MSAC lifetimes decrease with increasing ν , which is opposite to the trend that is seen in the nonadiabatic regime. The decrease of τ with increasing ν accelerates with increasing V; at V=2.75, the largest value studied, the lifetime ratio between $\nu=0$ and $\nu=10$ exceeds a factor of 1000. In order to understand this behavior, one may first compare the relative importance of the A- and B-coupling terms in the adiabatic representation. It is found in section 4.1 that the A-term is quite dominant. As a consequence, at sufficiently large V, the gradient of the trapped wave function, $\frac{\partial}{\partial x}\psi_u$, averaged over the wave-function extent, factors decisively into the nonadiabatic coupling strength. This means that, at the larger V-values, the lifetime should drop with increasing ν , as observed. Noting that wave-function gradient and classical velocity are related, the velocity dependence of the LZ equation predicts the same trend (see section 4.2).

Next, we discuss the deviations between the lifetimes obtained with the TDISE methods. For visibility of small deviations, we display the ratios $\tau_*/\tau_{\rm ad,FC}$ on a fine scale in figure 5(b). The adiabatic and nonadiabatic flux-calculation results agree very well in all regimes. We reiterate that $\tau_{\rm ad,FC}$ is still considered to be the most accurate and precise (see section 3.1). For $\tau_{\rm ad,FC} \gtrsim 200$, which roughly corresponds with $V \gtrsim 1$, the BW data also agree well. However, for $\tau_{\rm ad,FC} \lesssim 200$ they yield up to about 20% shorter lifetimes than the flux methods. It is also noted that the two BW results from the diabatic and adiabatic representations still agree very well with each other. The systematic deviation of the BW from the flux-calculation data at low V (nonadiabatic regime) may be attributed to the facts that at low V neighboring BW resonances begin to cross-talk, and that background phase slopes become a significant fraction of the slopes $d(\phi - \phi_0)/dW$ at the resonance centers (see figure 4(b)), rendering the BW data less accurate at low V. It is further seen that

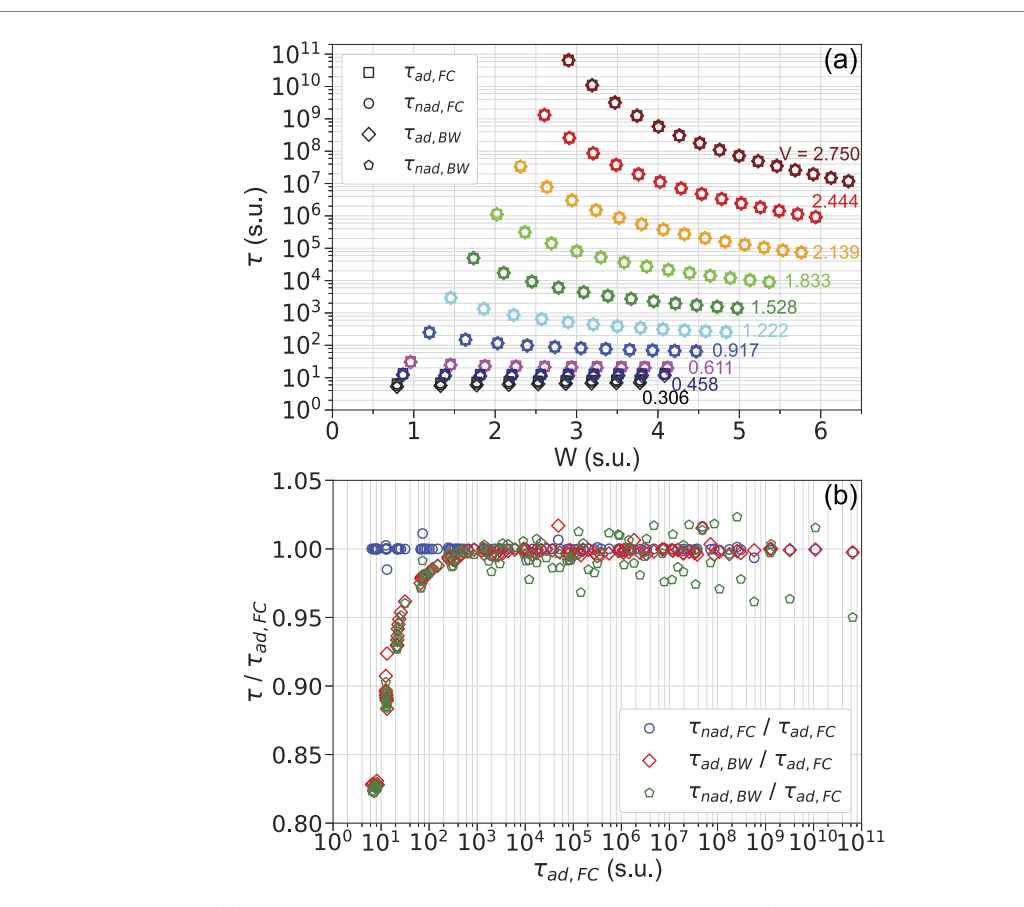


Figure 5. (a) Results of lifetime calculations using the methods indicated in the legend, for a range of values of the coupling strength V. The calculations cover all MSAC resonances that are less than about 3.8 scaled energy units above the adiabatic-potential minimum of V_u at x=0. (b) Ratios between the lifetimes shown in (a) and $\tau_{\rm ad,FC}$ vs $\tau_{\rm ad,FC}$. The plot includes data points for all V- and ν -values also shown in (a).

the numerical noise of the diabatic BW calculations can reach 5% at large V, where the resonances become extremely narrow and the computation of the slopes $d(\phi-\phi_0)/dW$ becomes less accurate. Notwithstanding, the overall good agreement, seen on the fine scale in figure 5(b), validates methods and results across the entire V- and ν -regimes studied.

4. Approximation methods

4.1. Perturbation theory

The adiabatic representation lends itself to a perturbative description of nonadiabatic decay [13, 42]. In this approach, we find bound MSACs on $\tilde{V}_u(x)$ used in equation (6), neglecting the nonadiabatic A- and B-couplings (but keeping the diagonal B-terms). These states differ from the true MSACs in that they are infinitely-long-lived, and in that their energies, $W_{\nu,FGR}$, are up to 0.07 s.u. below the true resonance energies, W_{ν} . The energy deviations are most notable at small coupling V, where the off-diagonal nonadiabatic terms are large and cause the largest shifts $W_{\nu}-W_{\nu,FGR}$. We denote the wave functions of the coupling- and decay-free approximations of the MSACs as $\psi_{u,\nu,FGR}(x)$. The $\psi_{u,\nu,FGR}(x)$ are weakly coupled to the continuum of free-particle states on the potential $\tilde{V}_d(x)$. The solutions on $\tilde{V}_d(x)$ are, asymptotically, identical with Airy functions [37]. Factoring in that on $\tilde{V}_d(x)$ the wave functions extend to both $\pm\infty$, as opposed to just one side on a linear potential, we normalize the free states such that the amplitude of their oscillatory tails at large positive x is

$$\psi_{d,W,FGR}(x) \approx \sqrt{\frac{1}{\pi}} |x + 2W|^{-1/4}.$$
 (12)

There, W is the level energy. The solutions $\psi_{d,W,\text{FGR}}(x)$ normalized in that way are orthonormal in unit energy, i.e. it is $\langle \psi_{d,W',\text{FGR}} | \psi_{d,W,\text{FGR}} \rangle = \delta(W-W')$. According to FGR, the transition rate from $|\psi_{u,\nu,\text{FGR}}\rangle$ to $|\psi_{d,W,\text{FGR}}\rangle$ then is given by $\Gamma_{\text{FGR}} = 2\pi |M|^2$, with a matrix element

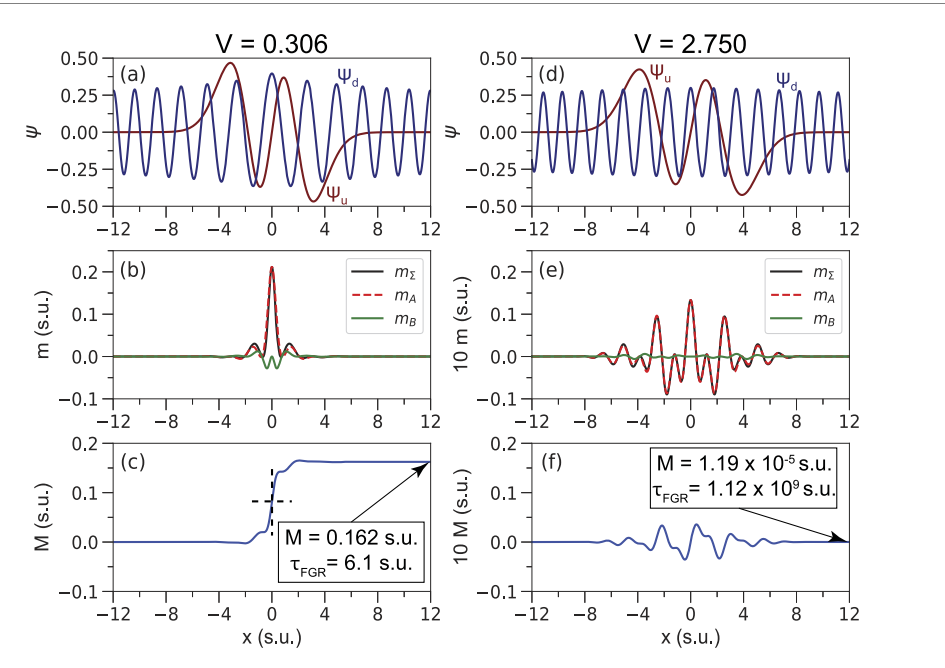


Figure 6. (a) and (d) Wave functions $\psi_u(x)$ and $\psi_d(x)$ for MSAC $\nu=3$ at V=0.306 and V=2.75, respectively. (b) and (e) Transition amplitudes $m_A(x)$, $m_B(x)$ and $m_\Sigma(x)$, defined in the text, for the states in (a) and (d), respectively. (c) and (f) $M(x) = \int^x m_\Sigma(x') dx'$ for the states in (a) and (d), respectively. The transition matrix element M in FGR, given by M(x) at the right margins, and the FGR lifetimes for the state, τ_{FGR} , are indicated in the boxes. Note the magnified y-scales in (e) and (f).

$$M = \langle \psi_{d,W,FGR} | \hat{B}_{du} + i \hat{A}_{du} \hat{p}_x | \psi_{u,\nu,FGR} \rangle$$

$$= \int \psi_d^*(x) \left[B_{du}(x) + A_{du}(x) \frac{d}{dx} \right] \psi_u(x) dx, \tag{13}$$

where we abbreviate $\psi_u(x) = \langle x | \psi_{u,\nu,\text{FGR}} \rangle$ and $\psi_d(x) = \langle x | \psi_{d,W,\text{FGR}} \rangle$. The free-particle energy in the integral equals that of the quasi-bound state, $W = W_{\nu,\text{FGR}}$. Also, here all $\psi(x)$ are real, and the integration range is limited by the range of $\psi_u(x)$. Since in the present problem $B_{du}(x)$ and d/dx have odd and $A_{du}(x)$ has even parity in x, even $\psi_u(x)$ decay into odd solutions $\psi_d(x)$ and vice versa. The FGR lifetimes then are

$$\tau_{\text{FGR}} = 1/(2\pi |M|^2).$$
 (14)

The FGR calculation is visualized in figure 6 for a small and a large V-value, for the case $\nu=3$. While the bound and free wave functions, $\psi_u(x)=\langle x|\psi_{u,\nu=3,FGR}\rangle$ and $\psi_d(x)=\langle x|\psi_{d,W,FGR}\rangle$, look quite similar in the two cases (see figures 6(a) and (d)), the coupling matrix elements are very different. We define the matrix-element 'densities' $m_A(x)=\psi_d(x)A_{du}(x)\frac{\mathrm{d}}{\mathrm{d}x}\psi_u(x)$, $m_B(x)=\psi_d(x)B_{du}(x)\psi_u(x)$, and the coherent sum $m_\Sigma(x)=m_A(x)+m_B(x)$, and display these functions in figures 6(b) and (e). For V=0.306 the m-densities are large, localized to within just the central lobe of $\psi_u(x)$, and largely uni-polar, whereas for V=2.75 the m-densities are weak, spread-out over the entire reach of $\psi_u(x)$, highly oscillatory and bi-polar. In both cases, $m_A(x)$ is much larger than $m_B(x)$ in magnitude, on average. As a result, for small V the nonadiabatic decay is fast and largely driven by couplings localized to within a small, interior region of $\psi_u(x)$, whereas for large V the nonadiabatic decay is slow and spread-out over the entire range of $\psi_u(x)$. These observations validate statements that we have made in section 3.2 with regard to the ν -dependence of the MSAC lifetimes in different regimes of V.

In figures 6(c) and (f) we show the integrals of m(x), whose asymptotic values, $M=M(x_{\max})$, give the FGR lifetimes according to equation (14). Due to symmetry, the integral M(x) has odd parity about a symmetry point at x=0 (crosshair in figure 6(c)), and it is $M=M(x_{\max})=2M(x=0)$. For low and moderate values of V, the large amplitudes and the somewhat uni-polar characteristics of m(x) lead to numerically stable results for M and τ_{FGR} . At large V, however, the integral in equation (13) is numerically challenging because of the bipolar and highly oscillatory behavior of $m_{\Sigma}(x)$. It is seen in figure 6(f) that at large V the integral $M=\int m_{\Sigma}(x)\mathrm{d}x$ comes down to a very small, nearly-vanishing remainder after integration, as evidenced by the fact that M(x) has a near-perfect zero crossing at x=0, leading to a very small matrix element M. To get converging values for M, at the largest V-values studied we had to decrease the spatial step size in the wave-function computations and in the integral for M by a factor of up to about

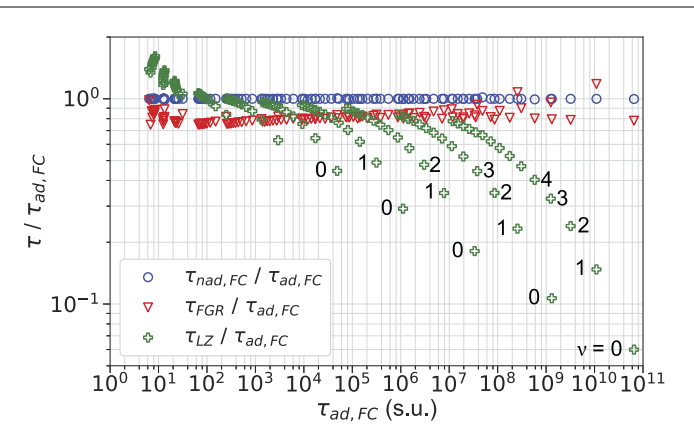


Figure 7. Ratios between lifetimes from a perturbative calculation based on FGR, $\tau_{\rm FGR}$, and from the semi-classical LZ approximation, $\tau_{\rm LZ}$ (see section 4.2), divided by the lifetime $\tau_{\rm ad,FC}$ from the non-perturbative calculation, versus $\tau_{\rm ad,FC}$. For reference, we also show $\tau_{\rm nad,FC}/\tau_{\rm ad,FC}$. The data points encompass all MSACs also shown in figure 5. Numbers next to the LZ data points with the largest deviations are vibrational quantum numbers, ν .

100 relative to the step size used in the non-perturbative methods. Nevertheless, even at the largest V considered the FGR computations are still quite fast because the wave functions to be computed are scalar.

In figure 7 we present the ratio $\tau_{\rm FGR}/\tau_{\rm ad,FC}$ for all values of V and ν also shown in figure 5. As in figures 3(b) and 5(b), $\tau_{\rm ad,FC}$ is used as a reference because the non-perturbative adiabatic wave-function flux calculation is the most accurate and precise. The lifetime ratios are plotted on a log scale covering about two decades, which is fine enough to observe relative deviations as small as about 1% and wide enough to also cover relative deviations for a LZ model (see section 4.2). The $\tau_{\rm FGR}/\tau_{\rm ad,FC}$ -ratios, plotted in figure 7 versus $\tau_{\rm ad,FC}$, follow a quite well-defined trend line at 0.1 to 0.3 below unity, with the lowest deviations occurring in the nonadiabatic and adiabatic limits on the left and right margins of the plot, respectively. At the largest $\tau_{\rm ad,FC}$ -values, corresponding to large V- and low ν -values, there is additional numerical noise on the order of ± 0.1 , caused by the delicate nature of the M-matrix elements at large V (see figure 6 and related discussion).

The FGR approach in this work differs from typical applications of FGR in which the wave functions are perturbation-independent, and the perturbation has a tunable strength. In contrast, in the present case the perturbation V is fixed for a given set of wave functions $\psi_u(x)$ and $\psi_d(x)$, and the wave functions themselves depend on the fixed perturbation V (via the diagonal B-terms included in \tilde{V}_u and \tilde{V}_d). The matrix-element densities m(x) have a complex spatial structure and are in first order only. The deviations of the FGR from the non-perturbative results are notable, albeit not exceeding about 30%. A practical concern relies in the fact that at large V the spatial step size in the FGR calculation of the matrix element M has to be set very small to achieve convergence, due to the delicate nature of the M-integral at large V (see figure 6).

4.2. Landau-Zener model

For a semi-classical estimate of MSAC lifetimes using the LZ equation, we use a LZ tunneling 'attempt rate' of twice the vibrational frequency, which gives an attempt rate of $R = (W_{\nu+1} - W_{\nu-1})/\pi$ (s.u.). The LZ coupling equals V and the differential slope of the diabatic potentials equals s = 1, in s.u.. For a fixed particle velocity, v, the LZ tunneling probability is $P_{\rm LZ} = \exp(-2\pi V^2/(s\nu))$, and the lifetime $\tau_{\rm LZ} = 1/(RP_{\rm LZ})$, in s.u.. Assuming that a semi-classical picture with a point-particle velocity v suffices to describe the quantum problem of interest, one still needs a rule for how to get v. From Fourier transforms of MSAC wave functions in any representation (diabatic or adiabatic), one expects and finds that v could be on the order of $\sqrt{W_{\nu} - V}$, which also accords with the classical virial theorem for a harmonic oscillator. Further, classically the velocity peaks at $v = \sqrt{2(W_{\nu} - V)}$ at the crossing. For the largest V and lowest v studied in this work, these v-values produce $\tau_{\rm LZ}$ -values that are about 20 orders of magnitude too long. As the exponent in the LZ tunneling probability is $\infty - 1/v$, we may surmise that the high-velocity wings in the Fourier transforms of the MSAC wave functions govern the LZ decay rate. Empirically, one finds that $v = \sqrt{2W_{\nu}}$, used in the following, overall leads to the best LZ estimates for the MSAC lifetimes (that can still be several orders of magnitude off).

The deviations of $\tau_{\rm LZ}$ from quantum calculations are shown in figure 7 in terms of $\tau_{\rm LZ}/\tau_{\rm ad,FC}$. It is seen that, over our range in V and ν studied, the LZ model may serve as a very rough guideline to predict MSAC lifetimes, as the $\tau_{\rm LZ}$ -values stay within a factor of about 20 from $\tau_{\rm ad,FC}$. The inaccuracy of the $\tau_{\rm LZ}$ -values accelerates in the adiabatic region (large $\tau_{\rm ad,FC}$). The strong ν -dependence of $\tau_{\rm LZ}/\tau_{\rm ad,FC}$, seen especially in the adiabatic region, reiterates that we have no well-founded rule for the classical velocity v. As such, the

poor overall agreement of $\tau_{\rm LZ}$ with the quantum results reflects the fact that a semi-classical model applied on a problem that is in the quantum domain of the vibrational motion is not necessarily accurate.

Considering quantum—classical correspondence, we add that with increasing ν our model system becomes more classical, and with decreasing V the nonadiabatic transitions become relatively well-localized in the spatial region near x=0. As a result, for $V\lesssim 1$, and for $V\gtrsim 1$ and ν exceeding a V-dependent limit evident from figure 7, the $\tau_{\rm LZ}$ -values deviate by less than about 50% from the corresponding $\tau_{\rm ad,FC}$ -values, and the agreement improves with increasing ν . These observations accord with the expectation that quantum and classical results should converge in these limits.

5. Conclusion

We have computed nonadiabatic lifetimes of metastable states on symmetric avoided crossings. Among six non-perturbative quantum methods, the results of which generally agree well, a wave-function flux method implemented in the adiabatic representation is the most accurate and precise, with lifetime uncertainties estimated at about 1%. Using the given relations between scaled and physical units, the results presented in figure 5(a) are portable to a variety of applications, including Rydberg molecules [23, 25] and atom trapping and guiding on dressed potentials [12].

In addition to providing accurate, non-perturbative lifetime data, our comparisons have shown that time-dependent perturbation theory in first order, applied to states in the adiabatic representation, with the off-diagonal nonadiabatic terms treated as a perturbation, yields approximate lifetimes that deviate by less than about 30% from the non-perturbative values. Semi-classical estimates based on the LZ tunneling formula were generally found to be quite inaccurate. The inaccuracy is largest for vibrational ground states in the adiabatic (long-lifetime) regime, which is the case of greatest relevance in atom trapping and guiding. Expanding on earlier works in atom trapping [13] and Rydberg molecules [29], the non-perturbative methods tested in the present work can be generalized to problems with more than two adiabatic potentials with non-linear spatial dependence and variable mutual couplings.

Additionally, nonadiabatic lifetimes of metastable states on conical intersections [43–46] may be of interest in quantum chemistry. A minimal, two-dimensional model of a conical intersection with spatial coordinates x and y has a diabatic Hamiltonian

$$\hat{H}_{\mathrm{D,2D}} = -rac{1}{2} \left(egin{array}{ccc} rac{\partial^2}{\partial x^2} + rac{\partial^2}{\partial y^2} & 0 \ 0 & rac{\partial^2}{\partial x^2} + rac{\partial^2}{\partial y^2} \end{array}
ight) + rac{1}{2} \left(egin{array}{ccc} -x & eta y \ eta y & x \end{array}
ight),$$

with a constant β . Holding the *y*-coordinate constant, the problem coincides with that of an anti-crossing, considered in our present work. However, dynamics along the *y*-degree of freedom connects the quantum solutions with the true degeneracy point at x = y = 0, which will fundamentally alter the physics of nonadiabatic decay of states on the upper potential energy surfaces. Future work may address this topic, as well as the role of curvatures of diabatic potentials.

Acknowledgments

The work was supported by the NSF Grant No. PHY-2110049 and in part through computational resources and services provided by Advanced Research Computing at the University of Michigan, Ann Arbor.

Data availability statement

The data that support the findings of this study are available upon reasonable request from the authors.

ORCID iDs

Alisher Duspayev https://orcid.org/0000-0001-5322-5762 Georg Raithel https://orcid.org/0000-0002-2005-8440

References

- [1] Nakamura H 2012 Nonadiabatic Transition: Concepts, Basic Theories, and Applications (Singapore: World Scientific)
- [2] Tully J C 2004 Concluding remarks Faraday Discuss. 127 463-6
- [3] Zhang R, Morrow N V, Berman P R and Raithel G 2005 Laser cooling in an optical lattice that employs Raman transitions Phys. Rev. A 72 043409
- [4] Lundblad N, Lee P J, Spielman I B, Brown B L, Phillips W D and Porto J V 2008 Atoms in a radio-frequency-dressed optical lattice Phys. Rev. Lett. 100 150401
- [5] Pan J-S, Zhang W, Yi W and Guo G-C 2016 Bose–Einstein condensate in an optical lattice with Raman-assisted two-dimensional spin–orbit coupling *Phys. Rev.* A 94 043619
- [6] Anderson R P, Trypogeorgos D, Valdés-Curiel A, Liang Q-Y, Tao J, Zhao M, Andrijauskas T, Juzeliūnas G and Spielman I B 2020 Realization of a deeply subwavelength adiabatic optical lattice *Phys. Rev. Res.* 2 013149
- [7] Leanhardt A E, Chikkatur A P, Kielpinski D, Shin Y, Gustavson T L, Ketterle W and Pritchard D E 2002 Propagation of Bose–Einstein condensates in a magnetic waveguide *Phys. Rev. Lett.* 89 040401
- [8] Zobay O and Garraway B M 2004 Atom trapping and two-dimensional Bose–Einstein condensates in field-induced adiabatic potentials Phys. Rev. A 69 023605
- [9] White M, Gao H, Pasienski M and DeMarco B 2006 Bose–Einstein condensates in RF-dressed adiabatic potentials Phys. Rev. A 74 023616
- [10] Hofferberth S, Fischer B, Schumm T, Schmiedmayer J and Lesanovsky I 2007 Ultracold atoms in radio-frequency dressed potentials beyond the rotating-wave approximation *Phys. Rev.* A 76 013401
- [11] Colombe Y, Knyazchyan E, Morizot O, Mercier B, Lorent V and Perrin H 2004 Ultracold atoms confined in rf-induced two-dimensional trapping potentials *Europhys. Lett.* **67** 593–9
- [12] Garraway B M and Perrin H 2016 Recent developments in trapping and manipulation of atoms with adiabatic potentials *J. Phys. B: At. Mol. Opt. Phys.* 49 172001
- [13] Burrows K A, Perrin H and Garraway B M 2017 Nonadiabatic losses from radio-frequency-dressed cold-atom traps: beyond the Landau–Zener model Phys. Rev. A 96 023429
- [14] Hänsel W, Reichel J, Hommelhoff P and Hänsch T W 2001 Trapped-atom interferometer in a magnetic microtrap Phys. Rev. A 64 063607
- [15] Sherlock B E, Gildemeister M, Owen E, Nugent E and Foot C J 2011 Time-averaged adiabatic ring potential for ultracold atoms Phys. Rev. A 83 043408
- [16] Vangeleyn M, Garraway B M, Perrin H and Arnold A S 2014 Inductive dressed ring traps for ultracold atoms J. Phys. B: At. Mol. Opt. Phys. 47 071001
- [17] Navez P, Pandey S, Mas H, Poulios K, Fernholz T and von Klitzing W 2016 Matter-wave interferometers using TAAP rings New J. Phys. 18 075014
- [18] Raithel G, Benson O and Walther H 1995 Atomic interferometry with the micromaser Phys. Rev. Lett. 75 3446–9
- [19] Haroche S 2013 Nobel lecture: controlling photons in a box and exploring the quantum to classical boundary *Rev. Mod. Phys.* **85** 1083–102
- [20] Rubbmark J R, Kash M M, Littman M G and Kleppner D 1981 Dynamical effects at avoided level crossings: a study of the Landau–Zener effect using Rydberg atoms Phys. Rev. A 23 3107–17
- [21] Gallagher T F 2005 Rydberg Atoms vol 3 (Cambridge: Cambridge University Press)
- [22] Reinhard A, Cubel Liebisch T, Knuffman B and Raithel G 2007 Level shifts of rubidium Rydberg states due to binary interactions Phys. Rev. A 75 032712
- [23] Shaffer J P, Rittenhouse S T and Sadeghpour H R 2018 Ultracold Rydberg molecules Nat. Commun. 9 1965
- [24] Hollerith S, Zeiher J, Rui J, Rubio-Abadal A, Walther V, Pohl T, Stamper-Kurn D M, Bloch I and Gross C 2019 Quantum gas microscopy of Rydberg macrodimers Science 364 664-7
- [25] Fey C, Hummel F and Schmelcher P 2020 Ultralong-range Rydberg molecules Mol. Phys. 118 e1679401
- [26] Duspayev A, Han X, Viray M A, Ma L, Zhao J and Raithel G 2021 Long-range Rydberg-atom—ion molecules of Rb and Cs *Phys. Rev. Res.* 3 023114
- [27] Deiß M, Haze S and Hecker Denschlag J 2021 Long-range atom-ion Rydberg molecule: a novel molecular binding mechanism Atoms 9 34
- [28] Zuber N, Anasuri V S V, Berngruber M, Zou Y-Q, Meinert F, Löw R and Pfau T 2021 Spatial imaging of a novel type of molecular ions (arXiv:2111.02680)
- [29] Duspayev A and Raithel G 2022 Nonadiabatic decay of Rydberg-atom-ion molecules Phys. Rev. A 105 012810
- [30] Landau L 1932 Zur Theorie der Energieübertragung. II Phys. Z. Sowjetunion 2 46-51
- [31] Zener C 1932 Non-adiabatic crossing of energy levels Proc. R. Soc. A 137 696
- [32] Arnold C, Vendrell O, Welsch R and Santra R 2018 Control of nuclear dynamics through conical intersections and electronic coherences Phys. Rev. Lett. 120 123001
- [33] Hummel F, Keiler K and Schmelcher P 2021 Electric-field-induced wave-packet dynamics and geometrical rearrangement of trilobite Rydberg molecules Phys. Rev. A 103 022827
- [34] Hummel F, Eiles M T and Schmelcher P 2021 Synthetic dimension-induced conical intersections in Rydberg molecules Phys. Rev. Lett. 127 023003
- [35] Born M and Huang K 1954 Dynamical Theory of Crystal Lattices (New York: Oxford University Press)
- [36] Agostini F and Curchod B F E 2019 Different flavors of nonadiabatic molecular dynamics Wiley Interdiscip. Rev.-Comput. Mol. Sci. 9 e1417
- [37] Griffiths D J 2004 Introduction to Quantum Mechanics 2nd edn (Englewood Cliffs, NJ: Prentice-Hall)
- [38] Sakurai J J and Napolitano J 2017 Modern Quantum Mechanics 2nd edn (Cambridge: Cambridge University Press)
- [39] Muga J G, Palao J, Navarro B and Egusquiza I 2004 Complex absorbing potentials *Phys. Rep.* **395** 357–426
- [40] Koonin S E and Meredith D C 1990 Computational Physics Fortran Version (Reading, MA: Addison-Wesley) pp 169–80
- [41] Duspayev A and Raithel G 2021 Tractor atom interferometry Phys. Rev. A 104 013307
- [42] Mandal A and Hunt K L C 2018 Quantum transition probabilities during a perturbing pulse: differences between the nonadiabatic results and Fermi's golden rule forms J. Chem. Phys. 148 194107

- [43] Yarkony D R 1996 Diabolical conical intersections *Rev. Mod. Phys.* **68** 985–1013
- [44] Matsika S and Krause P 2011 Nonadiabatic events and conical intersections Annu. Rev. Phys. Chem. 62 621-43
- [45] Domcke W, Yarkony D R and Köppel H 2011 Conical Intersections: Theory, Computation and Experiment vol 17 (Singapore: World Scientific)
- [46] Malhado J P and Hynes J T 2016 Non-adiabatic transition probability dependence on conical intersection topography *J. Chem. Phys.* **145** 194104